Cathodic electrosynthesis of ZnMn2O4/Mn3O4 composite nanostructures for high performance supercapacitor applications

Accepted Manuscript

Cathodic electrosynthesis of $ZnMn_2O_4/Mn_3O_4$ composite nanostructures for high performance supercapacitor applications

Bahareh Ameri, Saied Saeed Hosseiny Davarani, Hamid Reza Moazami, Hamideh Darjazi

PII: S0925-8388(17)31888-1

DOI: 10.1016/j.jallcom.2017.05.271

Reference: JALCOM 42002

To appear in: *Journal of Alloys and Compounds*

Received Date: 28 March 2017

Revised Date: 25 May 2017

Accepted Date: 26 May 2017

Please cite this article as: B. Ameri, S.S.H. Davarani, H.R. Moazami, H. Darjazi, Cathodic electrosynthesis of $ZnMn_2O_4/Mn_3O_4$ composite nanostructures for high performance supercapacitor applications, *Journal of Alloys and Compounds* (2017), doi: 10.1016/j.jallcom.2017.05.271.

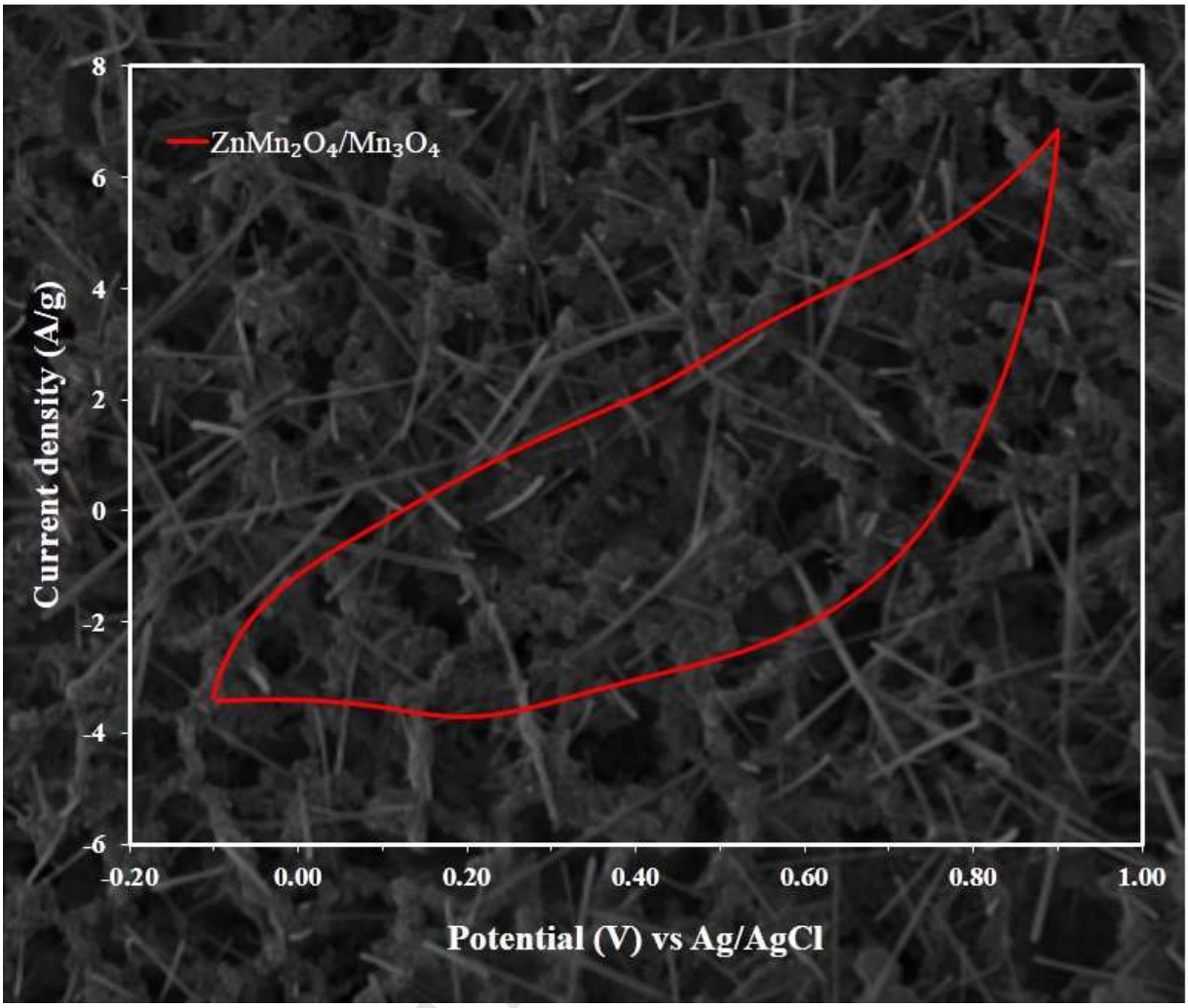

Cathodic electrosynthesis of $ZnMn_2O_4/Mn_3O_4$ composite nanostructures for high performance supercapacitor applications

Bahareh Ameri[a], Saied Saeed Hosseiny Davarani[*a], Hamid Reza Moazami[b], Hamideh Darjazi[C]

[a] Faculty of Chemistry, Shahid Beheshti University, G. C., 1983963113, Evin, Tehran, Iran

[b] Physics and Accelerators Research School, NSTRI, P. O. Box 14395-836, Tehran, Iran

[c] Department of Materials Engineering, NaghsheJahan Institute of Higher Education, Baharestan, Isfahan, Iran

***Corresponding author:** Tel.: +98 21 22431667; Fax: +98 21 22431663.

E-mail: ss-hosseiny@sbu.ac.ir (S.S.H. Davarani).

Abstract

$ZnMn_2O_4/Mn_3O_4$ composite nanostructures were prepared by cathodic electrodeposition followed by heat treatment. A mixed hydroxide precursor was galvanostatically electrodeposited from aqueous solution containing Mn and Zn (as nitrates) and the obtained precursor was annealed to prepare the composite. This composite exhibited much better electrochemical behaviors than bare Mn_3O_4. Rietveld analysis of the X-ray diffraction (XRD) data showed that the product was composed of Mn_3O_4, $ZnMn_2O_4$ and minor amounts of λ-MnO_2. Furthermore, the obtained composite was characterized by Fourier transform infrared spectrometry (FT-IR) and energy dispersive spectrometry (EDS). Field emission scanning electron micrographs (FE-SEM) and transmission electron micrographs (TEM) revealed co-existence of nanoparticles and high aspect ratio nanorods. Electrochemical performance and ion transport of $ZnMn_2O_4/Mn_3O_4$ composite were studied via galvanostatic charge-discharge (GCD) cycling and electrochemical impedance spectroscopy (EIS). Cyclic voltammetric (CV) measurements showed a maximum specific capacitance of 321.34 F/g at the scan rate of 1 mV/s. 93% of this specific capacitance was retained after 2000 cycles.

Keywords: $ZnMn_2O_4$; Mn_3O_4; Electrosynthesis; Nanorods; Supercapacitor

1. Introduction

The rich chemistry of manganese oxides has aroused interest in various scientific fields such as catalysis [1], ion exchange [2], magnetic/electromagnetic [3, 4] and energy storage materials [5]. As energy producing materials, manganese oxides have a long history that goes back to the discovery of Laclanche cells in 1866. Laclanche cells have been replaced by more efficient ones in many applications. However, recent works have proposed an emerging application for manganese oxides as energy storage materials [6, 7]. These are necessary parts of future energy production facilities that secure a sustainable supply of energy from renewable sources of discrete nature. Supercapacitors have been identified as a new generation of efficient energy storage devices due to their long cycle life, high power density, and rapid charge-discharge rate. Transition metal oxides with different oxidation states are widely used as electrode materials in supercapacitors where the charge is stored through internal redox reactions. High abundance, environmental friendliness, different oxidation states, and low cost make manganese oxides suitable candidates for supercapacitor applications. Hitherto, various strategies have been applied to improve the storage ability of MnO_x including morphological modification [8, 9], composite/hybrid formation, and doping [10, 11]. Among the various forms of manganese oxide, Mn_3O_4 (hausmannite) is one of the most stable forms which has specifically been considered as an electrode material in supercapacitors. In the reverse spinel structure of hausmannite, manganese simultaneously exists in two oxidation states (Mn^{2+} and Mn^{3+}). Although, Mn_3O_4 nanostructures exhibit a good storage ability in a relatively broad potential window but the specific capacitance values are far below theoretic values. High specific capacitance of hausmannite is bottlenecked by its low inherent electrical conductivity [12]. At the nanoscale, special properties appear to improve electrical, optical, chemical, and mechanical characteristics [13]. The physical and chemical properties of nanomaterials are related to their particle sizes and morphologies.

Various methods for the synthesis of Mn_3O_4 nanostructures such as thermal decomposition [4], hydrothermal [14]/solvothermal synthesis [15], sol–gel technique [16] and sono-chemical synthesis [17] have been reported. Unfortunately, most of these techniques are destructive to the environment because of their toxic solvents and reducing agents which should be replaced by green ones.

$ZnMn_2O_4$ has been widely studied as an electrode material for lithium ion batteries [18]. Some researchers have proposed $ZnMn_2O_4$ as a supercapacitor material but its reported specific capacitance values are around 160 F/g [19, 20] which are relatively low with respect to other binary/ternary transition metal oxides. On the other hand, $ZnMn_2O_4$ nanorods demonstrate a high electrical conductivity making it suitable material for solid oxide fuel cells [21] and microwave dielectrics for low-temperature co-fired ceramics (LTCC) technology [22, 23]. The high electrical conductivity of $ZnMn_2O_4$ is attributed to high mobility of Zn in the structure [24]. The idea behind this work was to prepare a $ZnMn_2O_4/Mn_3O_4$ composite in order to take advantage of high conductivity of $ZnMn_2O_4$ and high specific capacitance of Mn_3O_4.

In this study, for the first time, $ZnMn_2O_4/Mn_3O_4$ composite nanostructures were synthesized by a facile, green, and controllable cathodic electrodeposition method. The synthesis route comprises galvanostatic generation of base in a mixed Zn/Mn nitrate solution at a Zn/Mn ratio of 10%. The electrogenerated base causes deposition of a mixed hydroxide precursor which is then heat treated to prepare $ZnMn_2O_4/Mn_3O_4$ composite. XRD patterns confirmed the presence of $ZnMn_2O_4$ and Mn_3O_4, along with minor amounts of λ-MnO_2. The FE-SEM and TEM micrographs showed dual nanorods/nanoparticle morphology of the prepared composite. Back scattered electron (BSE) images revealed that the nanorods are more likely to be $ZnMn_2O_4$. The electrochemical behavior and charge storage ability of the prepared composite were examined by CV, GCD and EIS measurements.

2. Experimental

2.1 Materials

$Mn(NO_3)_2.4H_2O$ and $Zn(NO_3)_2.6H_2O$ were purchased from Merck (Darmstadt, Germany). Deionized water was obtained by a Millipore water purification system (Milford, MA, USA).

2.2 Preparation of $ZnMn_2O_4/Mn_3O_4$

The starting solution consisted of Mn^{2+} (10^{-2} M) freshly prepared by dissolving $Mn(NO_3)_2.4H_2O$ in deionized water. Zn^{2+} was added as $Zn(NO_3)_2.6H_2O$ at Zn to Mn molar ratios of 0 and 10%. The electrodeposition was performed in a 1 L cubic glass container with a common 100×100×0.5 mm steel 316 L planar cathode in the center and two parallel planar graphite anodes of the same dimensions placed on both sides of the cathode. The electrodeposition was performed under a galvanostatic regime at the current density of 0.75 mA/cm^2 and total charge of 2 coulombs per square centimeter of the cathode area. The cathode was removed from the solution, washed frequently with deionized water and allowed to dry in air for 12 h. The electrodeposited layer was then scrapped from the cathode surface and heat treated in a temperature program including the rise of temperature from 25 to 300 ^{0}C at the heating rate of 10^0C/min.

2.3 Characterization

The crystalline structure of the samples was studied by X-ray diffraction (XRD) analysis by means of a STOE XD-3A X-ray diffractometer using CuK_α line at λ=1.5406 nm. The morphology and elemental composition of the samples were investigated using a TESCAN VEGA3 SB field-emission scanning electron microscope (FE-SEM) equipped with an energy dispersive spectrometry (EDS) detector and transmission electron microscope (TEM, Zeiss-

EM10C). A BOMEM MB-series FT-IR spectrometer was used to record the FT-IR spectra of the samples in KBr media within the wave number range of 250-4000 cm^{-1}.

2.4 Electrochemical measurements

Electrochemical measurements were carried out using an ORIGAFLEX-OGF500 (France) in the frequency range of 100 kHz to 0.01 Hz. Cyclic voltammograms were recorded in Na_2SO_4 (1.0 M) aqueous solution within the potential range of -0.1 to +0.9 V vs Ag/AgCl in a standard three-electrode cell configuration with a platinum wire, an Ag/AgCl, and a glassy carbon (with 0.071 cm^2 area) as counter, reference and working electrodes, respectively. Specific Capacitance (SC) values were calculated by integration of current over the range of applied potential at different scan rates according to Eq. 1:

$$SC = \frac{1}{mv(V_a - V_c)} \int_{V_a}^{V_c} I(V)dV \quad (1)$$

where, I is the measured current (A), (V_a-V_c) is the sweep potential range (V), m is the mass of electrochemically active material (g), and v is the sweep rate (Vs^{-1}). The SC of the samples was also independently calculated from galvanostatic charge-discharge cycles at the constant current density of 1 mA/cm^2:

$$SC = \frac{I\Delta t}{m\Delta V} \quad (2)$$

where, SC is the specific capacitance (F/g), I is the discharge current (A), ΔV is the potential window (V), Δt is the discharge time (s), and m is the mass of electro-active material (g).

3. Results and discussion

3.1 Electrodeposition mechanism

There are various routes for the cathodic generation of base at the electrode surface according to the following reactions:

$$H_2O+2e^- \rightarrow H_2+2OH^- \qquad E^0= -1.05 \text{ V vs. Ag/AgCl} \qquad (3)$$

$$O_2+2H_2O+ 4e^- \rightarrow 4OH^- \qquad E^0= +0.18 \text{ V vs. Ag/AgCl} \qquad (4)$$

$$NO_3^-+H_2O+2e^- \rightarrow NO_2^-+2OH^- \qquad E^0= -0.21 \text{ V vs. Ag/AgCl} \qquad (5)$$

The generation of base brings about a local change in pH at the cathode surface which results in the precipitation of metallic ions and formation of hydroxide layer (Eq. 6):

$$Mn^{2+}+ 2OH^- \rightarrow Mn(OH)_2 \qquad K=Ksp^{-1} = 2.5\times10^{13} \qquad (6)$$

Firstly, the annealing of the resulting hydrous manganese hydroxide precursor yields hausmannite via a multistep solid phase reaction (Eq. 7):

$$Mn(OH)_2 \xrightarrow{\Delta} Mn(OOH) \xrightarrow[\text{Decay}]{\Delta} Mn_3O_4 \qquad (7)$$

In the next step and after the addition of Zn^{2+} to the solution, a uniform precipitation of mixed metal hydroxides ($Zn_m(OH)_n$, $Mn_p(OH)_q$) is formed on the surface of cathode electrode. Considering the values of solubility product constant (Ksp) at 25 °C for $Zn(OH)_2$ (3×10^{-16}) and $Mn(OH)_2$ (2.5×10^{-13}), the following equation can be proposed:

$$nZn^{2+} + mMn^{2+} + KOH^{-} \rightarrow Zn_nMn_m(OH)_k \quad (8)$$

Then, the heating step involved an oxidation reaction that converted the $Zn_nMn_m(OH)_k$ precursor into spinel $ZnMn_2O_4$ (Eq. 9):

$$Zn_nMn_m(OH)_k + \frac{1}{2}O_2 \rightarrow ZnMn_2O_4 + k/2H_2O \quad (9)$$

The concentrations of Zn^{2+} and Mn^{2+} in the initial solution were not in stoichiometric ratio of $ZnMn_2O_4$. Hence, the excess of Mn^{2+} ions formed Mn_3O_4 and, therefore, a $ZnMn_2O_4/Mn_3O_4$ composite was obtained.

3.2 X-ray diffraction analysis and Rietveld refinement

The cathodic base generation in Mn^{2+} baths is used to prepare manganese oxides with a great variety of morphology and crystalline forms. The X-ray diffraction was used to characterize the phase and crystal structure of the Mn_3O_4 sample (S1) and $ZnMn_2O_4/Mn_3O_4$ composite (S2). In this case, the Rietveld refinement is the most efficient method for determining crystalline phases, lattice parameters, and space group. The introduction of this technique has resolved the difficulties of other techniques with powder diffraction such as systematic overlapping of diffraction peaks because of symmetry conditions or significant background which reduces the accuracy of the results. The Rietveld method refines the parameters to achieve the best fit of experimental and calculated data by using a least squares fitting [25]. Fig. 1 presents the powder XRD patterns of the samples. The solid line displays the intensity of the calculated patterns and the dots indicate the observed intensity. As can be seen in Fig. 1a, the refinement results show the formation of a single phase spinel structure of Mn_3O_4 with tetragonal symmetry in the space group 141/amd and without any impurity peaks. The broad

reflection peaks reveal the smaller crystallite sizes of Mn_3O_4 with poor crystallinity. The area under the peak is used to calculate crystallinity according to Eq. 10.

$$\text{degree of crystallinity} = \frac{\text{sum of net area}}{\text{sum of total area}} * 100 \quad (10)$$

In the next step, Zn^{2+} was added to Mn^{2+} baths and $ZnMn_2O_4$ nanorods were formed on the substrate of Mn_3O_4 nanoparticles. This new phase demonstrates similar structures with Mn_3O_4 phase (tetragonal symmetry in the space group 141/amd). At $ZnMn_2O_4$ spinel phase, a portion of Zn^{2+} can be removed from the tetrahedral sites of $ZnMn_2O_4$ crystal structure to form λ-MnO_2 [26, 27]. This shows the cubic symmetry of manganese dioxide in the space group Fd3m. Fig. 1b illustrates the presence of crystalline phases very well. A complete expression used in Rietveld method to calculate the crystallite size is defined as:

$$FWHM^2 = (U + D^2_{st})(\tan^2\theta) + V(\tan\theta) + W + IG/\cos^2\theta \quad (11)$$

where U, V, and W are the usual peak shape parameters; IG is a measure of the isotropic size effect and D_{st} is the coefficient related to strain.

The main results from Rietveld refinements, crystallite size, and degree of crystallinity are shown in Table 1. The reliability R-factors containing profile residual R_p, weighted profile residual R_{wp}, and goodness of fit χ^2 confirmed the accuracy of the results [28].

3.3 The study of FT-IR

The prepared samples were characterized by FT-IR spectroscopy. As shown in Fig. 2, both samples have IR bands in the high frequency region of 3400 cm^{-1} and 1370 cm^{-1} corresponding to the stretching and bending vibrations of surface hydroxyl and adsorbed

atmospheric moisture on the surface of the nanomaterials, respectively. Both samples also showed prominent IR bands at 507 cm^{-1}, 630 cm^{-1}, and a shoulder at 710 cm^{-1}, which can be attributed to the stretching vibration of Mn^{3+} species in octahedral, tetrahedral sites, and the asymmetric vibration of Mn-O band in an octahedral environment, respectively. For $ZnMn_2O_4/Mn_3O_4$ sample, the shoulder disappeared and an additional peak emerged at 423 cm^{-1} which can be ascribed to the stretching vibration of Zn-O.

3.4 Morphology

The general morphology of the samples was examined by FE-SEM. The nanostructure electrodeposited from manganese nitrate solution (S1) possessed broken irregular nanosheets (Fig. 3a). The formation of nanosheets is attributed to 2D growth of electrodeposited layer in the dynamic template provided by the intense evolution of gaseous hydrogen. The addition of zinc in (S2) resulted in the formation of two co-existing nanostructures including nanoparticles and nanorods as depicted in Fig. 3b and Fig. 3c. The higher brightness of an individual nanorod in back scattered electron (BSE) micrograph of Fig. 3d suggested that the nanorods were composed of $ZnMn_2O_4$, whereas the nanoparticles were composed of Mn_3O_4. In the BSE mode of operation, the atoms of higher atomic number (Zn in this sample) reflect higher amount of electrons out of the specimen through elastic scattering [29]. The bell-shaped histograms of the particle size distribution according to FE-SEM images for $ZnMn_2O_4/Mn_3O_4$ composite are illustrated in Fig. 4. The highest diameter size distributions of nanoparticles and nanorods existing in the composite were observed in the range of 50-55 and 25-30 nanometer, respectively. The TEM was utilized for further investigation of the detailed structure of $ZnMn_2O_4/Mn_3O_4$ composite. As can be seen in Fig. 5, the TEM images of composite confirm the co-existence of nanoparticles and nanorods, which strongly support FE-SEM analysis.

The EDS spectra of the samples S1 and S2 are given in Fig. 6a and Fig. 6b, respectively. Quantitative elemental analysis showed that the Zn, Mn, and O contents in S2 were 3.59, 58.08 and 38.33%, respectively. The Zn/Mn ratio in the product was lower than that of the initial solution, indicating the partial leaching of Zn atoms from tetrahedral sites of $ZnMn_2O_4$ and forming λ-MnO_2.

3.5 Electrochemical properties

The investigation of the electrochemical performance of synthesized samples as electro-active electrodes was done by cyclic voltammetry (CV), galvanostatic charge-discharge measurements (GCD), and electrochemical impedance spectroscopy (EIS) in Na_2SO_4 aqueous solution (1.0 M). The three-electrode system included platinum electrode as auxiliary electrode, Ag/AgCl electrode as reference electrode, and a working electrode. To provide the working electrode, 85 wt% of the heat-annealed samples was mixed with 10 wt% acetylene black as the conducting material and 5 wt% of polyvinylidene fluoride (PVDF) as binder in N-methyl-2-pyrrolidone (NMP) solvent. The resulting paste was then pressed on the surface of the glassy carbon electrode and dried at 70˚C for 12h.

Fig. 7a shows the cyclic voltammetry (CV) curves of capacitive performance of the Mn_3O_4 and $ZnMn_2O_4/Mn_3O_4$ electrodes in the potential window of -0.1 to 0.9 V *vs* Ag/AgCl at the scan rate of 10 mV/s. As can be seen, current and storage capacity significantly enhanced with the addition of zinc and composite formation. Because of the 1D structure of $ZnMn_2O_4$ nanorods, diffusion of protons or alkaline ions into the structure becomes easier and faradic reactions perform better. The improvement of supercapacitor properties in composite mode is clearly seen by comparing the voltammograms (Fig. 7a). To further investigate, cyclic voltammetry curves of the Mn_3O_4 and $ZnMn_2O_4/Mn_3O_4$ electrodes were recorded at various

scan rates ranging from 1 to 50 mV/s (Fig. 7b and Fig. 7c). The shapes of CV curves proved the excellent electrochemical reversibility and ideal capacitive behavior of electro-active materials [30]. According to Eq. 1 from CV curves, the highest specific capacitances of $ZnMn_2O_4/Mn_3O_4$ composite and bare Mn_3O_4 were found to be 321.34 and 248.79 F/g, respectively, at the scan rate of 1 mV/s. The specific capacitance increases as scan rate goes down, so the lowest scan rate indicates the highest SC. In general, at higher scan rates, charge transfer is found to be low limiting the diffusion rate of electrolyte into the electrode materials because of decreasing the interaction between the electrolyte ions and electrode. However, at lower scan rates, the cations find time to easily penetrate throughout the electrode material. As a result, the capacitance is increased very much [31]. The SC values of 321.34, 246.13, 205.66, 169.56, 153.73, 139.98 and 131.97 F/g for $ZnMn_2O_4/Mn_3O_4$ composite and 248.79, 177.51, 132.38, 98.28, 84.78, 79.65 and 73.92 F/g for bare Mn_3O_4 were obtained using Eq. 1 at the scan rates of 1, 5, 10, 20, 30, 40 and 50 mV/s, respectively. These calculated specific capacitance values for both bare and composite forms were plotted versus scan rates as can be seen in Fig. 7d. The curves show that with increasing the scan rate, the SC of electrode materials reduced slowly. The capacitive storage ability of 131.97 F/g even at the scan rate of 50 mV/s confirms the high functionality of the supercapacitor.

To further evaluate the electrochemical performance of the Mn_3O_4 and $ZnMn_2O_4/Mn_3O_4$ electrodes, galvanostatic charge-discharge (GCD) tests were employed within the potential window of -0.1 to 0.9 V. Fig. 8a represents the charge-discharge curves at the current density of 1 A/g. With the addition of Zn^{2+} and the formation of composite, discharge time went up and SC value also increased according to Eq. 2. This is due to the special morphology of the $ZnMn_2O_4/Mn_3O_4$ composite which can lead to the considerable reduction of the diffusion length. The 1D structure of the observed nanorods facilitates the charge-discharge process and shows a better performance than the bare state with a 2D structure [32]. Fig. 8b and Fig.

8c show the charge-discharge curves of Mn_3O_4 and $ZnMn_2O_4/Mn_3O_4$ electrodes at different current densities ranging from 0.5 to 10 A/g, respectively. As current density rises, SC is reduced which can be due to the decreased efficient utilization of the active sites in the electrode material [14]. IR drop in these curves demonstrates faradic behavior of reaction which is in good agreement with the results of CV. With insertion and/or release of Na^+ into or out of the Mn_3O_4 structure, charge-discharge process can be obtained as follows [33, 34]:

$$Mn_3O_4 \text{ (spinel)} \rightarrow Na_\delta MnO_x.nH_2O \quad (12)$$

$$Na_\delta MnO_x.nH_2O + yH^+ + zNa^+ (y+z)\, e^- \leftrightarrow Na_{\delta+z}MnO_x.nH_2O \quad (13)$$

To further explore the electrochemical performance, two parameters of energy density (E, Wh/kg) and power density (P, W/Kg) using charge-discharge curves at different current densities were obtained by the following equations [35]:

$$E = \frac{CV^2}{2 * 3.6} \quad (14)$$

$$P = \frac{E}{t} \quad (15)$$

Fig. 8d shows a Ragone plot of the corresponding specific E versus P values for Mn_3O_4 and $ZnMn_2O_4/Mn_3O_4$ electrodes. As the energy densities reduce slowly with increasing power densities, the energy density of the $ZnMn_2O_4/Mn_3O_4$ electrode at the same power density is higher than that of Mn_3O_4 electrode which means that the $ZnMn_2O_4/Mn_3O_4$ composite exhibits a better performance.

The cycle stability of Mn_3O_4 and $ZnMn_2O_4/Mn_3O_4$ electrodes was studied for 2000 continuous CV cycles in 1.0 M Na_2SO_4 solution at the scan rate of 1 mV/s. As can be seen in

Fig. 9a, composite mode demonstrates a better cycling stability. 89% and 93% of initial specific capacitances were retained after 2000 cycles for Mn_3O_4 and $ZnMn_2O_4/Mn_3O_4$ electrodes, respectively. The improvement of cyclic stability in composite mode makes it suitable for practical applications.

In order to evaluate the ion transport mechanism, electrochemical impedance spectroscopy measurements (EIS) were performed at an open circuit potential with an ac perturbation of 5 mV in the frequency range of 100 kHz to 0.01 Hz. Fig. 9b shows the Nyquist plots and the equivalent circuit for Mn_3O_4 sample and $ZnMn_2O_4/Mn_3O_4$ composite. The equivalent circuit includes the solution resistance of R_s, the charge transfer resistance of R_{ct}, the double layer capacitance of C_{dl}, the pseudo capacitance of C_p, and the Warburg impedance of W (inset of Fig. 9b). The shape of the curves demonstrates the pseudo-capacitive behavior of the electrode materials. As shown in Fig. 9b, there are two distinct regions in the EIS spectra: 1) a semicircle at the high frequency region (R_{ct}), 2) a straight line at the low frequency region (W) [36]. Consistent with the previous results of the present work, the impedance decreased by increasing zinc and formation of composite compared with bare Mn_3O_4. The diameter of the semicircle for $ZnMn_2O_4/Mn_3O_4$ composite is much smaller (R_{ct}: 2.57 Ω) than that of Mn_3O_4 sample (R_{ct}: 0.76 Ω), which suggests that the composite mode possesses the lowest charge transfer resistance. This is because of the special morphology of nanorods which facilitate ion transfer throughout the structure and compensate the low conductivity of bare Mn_3O_4 [15].

A comparison of this work with previously reported fabrication methods and electrochemical performance of different Mn_3O_4 or composite electrodes for supercapacitors are given in Table 2.

4. Conclusion

In this work, $ZnMn_2O_4/Mn_3O_4$ composite nanostructures were synthesized by a facile cathodic electrodeposition method. The phase composition of the obtained composite was evaluated by Rietveld analysis of the XRD patterns. FE-SEM and TEM micrographs showed the unique architecture of the sample including Mn_3O_4 nanoparticles connected by $ZnMn_2O_4$ nanorods. Electrochemical tests including CV and GCD measurements revealed a significant improvement in the charge storage ability of the composite compared to that of Mn_3O_4 nanostructures synthesized in similar conditions. The highest specific capacitance values of 248.79 and 321.34 F/g were obtained for Mn_3O_4 and $ZnMn_2O_4/Mn_3O_4$ composite, respectively, at the scan rate of 1 mV/s. The improvement of the electrochemical behavior especially in the electrical conductivity for composite state was determined by EIS test. In fact, $ZnMn_2O_4$ with its high conductivity compensates the weakness of hausmannite. The composite retained 93% of its initial storage capacity after 2000 cycles, while this amount is 89% for bare Mn_3O_4. The high charge storage performance of the prepared sample, along with the simplicity and low cost of the synthesis route, justifies its viability as a supercapacitor material.

References

[1] J.K. Sharma, P. Srivastava, S. Ameen, M.S. Akhtar, G. Singh, S. Yadava, Azadirachta indica plant-assisted green synthesis of Mn_3O_4 nanoparticles: Excellent thermal catalytic performance and chemical sensing behavior, J. Colloid Interface Sci. 472 (2016) 220-228.

[2] Y.S. Kim, H. Kanoh, T. Hirotsu, K. Ooi, Chemical bonding of ion-exchange type sites in spinel-type manganese oxides $Li_{1.33}Mn_{1.67}O_4$, Mat. Res. Bull. 37 (2002) 391-396.

[3] Y. Wang, H. Guan, C. Dong, X. Xiao, S. Du, Y. Wang, Reduced graphene oxide (RGO)/Mn_3O_4 nanocomposites for dielectric loss properties and electromagnetic interference shielding effectiveness at high frequency, Ceram. Int. 42 (2016) 936-942.

[4] G. Wang, S. Wu, W. Zhou, Y. Wang, S. Li, Novel magnetic properties of single-crystalline Mn_3O_4 (0 0 4) film grown on $SrTiO_3$ (0 0 1) substrate by molecular beam epitaxy, Mater. Lett. 195 (2017) 86-88.

[5] J. Chen, X. Wu, Y. Gong, P. Wang, W. Li, Q. Tan, Y. Chen, Synthesis of Mn_3O_4/N-doped graphene hybrid and its improved electrochemical performance for lithium-ion batteries, Ceram. Int. 43 (2017) 4655-4662.

[6] G. Wang, L. Zhang, J. Zhang, A review of electrode materials for electrochemical supercapacitors, Chem. Soc. Rev. 41 (2012) 797-828.

[7] A. González, E. Goikolea, J.A. Barrena, R. Mysyk, Review on supercapacitors: Technologies and materials, Renew. Sust. Energ. Rev. 58 (2016) 1189-1206.

[8] H.R. Moazami, S.S.H. Davarani, T. Yousefi, A.R. Keshtkar, Synthesis of manganese dioxide nanosheets and charge storage evaluation, Mat. Sci. Semicon. Proc. 30 (2015) 682-687.

[9] J.-G. Wang, F. Kang, B. Wei, Engineering of MnO_2-based nanocomposites for high-performance supercapacitors, Prog. Mater. Sci. 74 (2015) 51-124.

[10] H.R. Moazami, S.S.H. Davarani, T. Yousefi, H. Darjazi, Iron mediated cathodic electrosynthesis of hausmannite nanoparticles, Mat. Sci. Semicon. Proc. 38 (2015) 240-248.

[11] H. Darjazi, S.S. Hosseiny Davarani, H.R. Moazami, T. Yousefi, F. Tabatabaei, Evaluation of charge storage ability of chrome doped Mn_2O_3 nanostructures derived by cathodic electrodeposition, Prog. Nat. Sci.: Mater. Int. 26 (2016) 523-527.

[12] S. Kulkarni, D. Puthusseri, S. Thakur, A. Banpurkar, S. Patil, Hausmannite manganese oxide cathodes for supercapacitors: Surface wettability and electrochemical properties, Electrochim. Acta 231 (2017) 460-467.

[13] O.R. Kakuee, V. Fathollahi, M. Lamehi-Rachti, P. Oliaiy, H. Seyedi, S. Safa, M. Mojtahedzadeh Larijani, H.R. Moazzami, Ion beam analysis of hydrogen-treated Ti/TiN protective nanomultilayers, Acta Phys. Pol. A 122 (2012) 132-137.

[14] D. Li, F. Meng, X. Yan, L. Yang, H. Heng, Y. Zhu, One-pot hydrothermal synthesis of Mn_3O_4 nanorods grown on Ni foam for high performance supercapacitor applications, Nanoscale Res. Lett. 8 (2013) 535-541.

[15] Y. Qiao, Q. Sun, J. Xi, H. Cui, Y. Tang, X. Wang, A modified solvothermal synthesis of porous Mn_3O_4 for supercapacitor with excellent rate capability and long cycle life, J. Alloys Compd. 660 (2016) 416-422.

[16] F. Nâamoune, B. Messaoudi, A. Kahoul, N. Cherchour, A. Pailleret, H. Takenouti, A new sol-gel synthesis of Mn_3O_4 oxide and its electrochemical behavior in alkaline medium, Ionics 18 (2012) 365-370.

[17] G.-R. Xu, X.-P. Min, Q.-L. Chen, Y. Wen, A.-P. Tang, H.-S. Song, Sonochemical synthesis of a Mn_3O_4/MnOOH nanocomposite for electrochemical energy storage, J. Alloys Compd. 691 (2017) 1018-1023.

[18] L.-X. Zhang, Y.-L. Wang, H.-F. Jiu, H.-y. Qiu, H.-y. Wang, Hollow core–shell $ZnMn_2O_4$ microspheres as a high-performance anode material for lithium-ion batteries, Ceram. Int., 41 (2015) 9655-9661.

[19] A. Sahoo, Y. Sharma, Synthesis and characterization of nanostructured ternary zinc manganese oxide as novel supercapacitor material, Mat. Chem. Phys. 149–150 (2015) 721-727.

[20] N. Guo, X.Q. Wei, X.L. Deng, X.J. Xu, Synthesis and property of spinel porous $ZnMn_2O_4$ microspheres, Appl. Surf. Sci. 356 (2015) 1127-1134.

[21] J.A. Kilner, J. Druce, T. Ishihara, in: M. Kendall, High-temperature solid oxide fuel cells for the 21st century, Second Edition, Academic Press, Boston, 2016, 85-132.

[22] Q.-S. Cao, W.-Z. Lu, X.-C. Wang, J.-H. Zhu, B. Ulla, W. Lei, Novel zinc manganese oxide-based microwave dielectric ceramics for LTCC applications, Ceram. Int. 41 (2015) 9152-9156.

[23] X.-K. Lan, Z.-Y. Zou, W.-Z. Lu, J.-H. Zhu, W. Lei, Phase transition and low-temperature sintering of $Zn(Mn_{1-x}Al_x)_2O_4$ ceramics for LTCC applications, Ceram. Int. 42 (2016) 17731-17735.

[24] N. Zhang, F. Cheng, Y. Liu, Q. Zhao, K. Lei, C. Chen, X. Liu, J. Chen, Cation-deficient spinel $ZnMn_2O_4$ cathode in $Zn(CF_3SO_3)_2$ electrolyte for rechargeable aqueous Zn-Ion battery J. Am. Chem. Soc. 138 (2016) 12894-12901.

[25] R. Safi, A. Ghasemi, R. Shoja-Razavi, E. Ghasemi, T. Sodaee, Rietveld structure refinement, cations distribution and magnetic features of $CoFe_2O_4$ nanoparticles synthesized by co-precipitation, hydrothermal, and combustion methods, Ceram. Int. 42 (2016) 6375-6382.

[26] J.C. Hunter, Preparation of a new crystal form of manganese dioxide: λ-MnO_2, J. Solid State Chem. 39 (1981) 142-147.

[27] L. Xue, Z.-S. Wu, C. Ge, X.-D. Zhang, Ultralow-temperature hydrothermal synthesis of Zn–Mn spinel nanocrystals: Its defect spinel of λ-MnO_2 prepared by a soft chemical method, Mat. Chem. Phys. 138 (2013) 124-130.

[28] S.O. Estrada, C.A. Huerta-Aguilar, T. Pandiyan, M. Corea, I.A. Reyes-Domínguez, G. Tavizon, Tuning of the magnetic response in cobalt ferrite $Co_xFe_{3-x}O_4$ by varying the Fe^{2+} to Co^{2+} molar ratios: Rietveld refinement and DFT structural analysis, J. Alloys Compd. 695 (2017) 2706-2716.

[29] J.I. Goldstein, D.E. Newbury, P. Echlin, D.C. Joy, C. Fiori, E. Lifshin, Scanning electron microscopy and X-ray microanalysis: A text for biologist, materials scientist, and geologists, Springer, US, Boston, MA, 1981, 123-204.

[30] M. Wang, H. Fei, P. Zhang, L. Yin, Hierarchically layered MoS_2/Mn_3O_4 hybrid architectures for electrochemical supercapacitors with enhanced performance, Electrochim. Acta 209 (2016) 389-398.

[31] P.T.M. Bui, J.-H. Song, Z.-Y. Li, M.S. Akhtar, O.B. Yang, Low temperature solution processed Mn_3O_4 nanoparticles: Enhanced performance of electrochemical supercapacitors, J. Alloys Compd. 694 (2017) 560-567.

[32] J. Xu, X. Fan, Q. Xia, Z. Shao, B. Pei, Z. Yang, Z. Chen, W. Zhang, A highly atom-efficient strategy to synthesize reduced graphene oxide-Mn_3O_4 nanoparticles composites for supercapacitors, J. Alloys Compd. 685 (2016) 949-956.

[33] B. Gnana Sundara Raj, A.M. Asiri, J.J. Wu, S. Anandan, Synthesis of Mn_3O_4 nanoparticles via chemical precipitation approach for supercapacitor application, J. Alloys Compd. 636 (2015) 234-240.

[34] J. Yang, X. Yang, Y.L. Zhong, J.Y. Ying, Porous MnO/Mn_3O_4 nanocomposites for electrochemical energy storage, Nano Energy 13 (2015) 702-708.

[35] A.A. Yadav, Influence of electrode mass-loading on the properties of spray deposited Mn_3O_4 thin films for electrochemical supercapacitors, Thin Solid Films 608 (2016) 88-96.

[36] B. Ameri, S.S.H. Davarani, R. Roshani, H.R. Moazami, A. Tadjarodi, A flexible mechanochemical route for the synthesis of copper oxide nanorods/nanoparticles/nanowires for supercapacitor applications: The effect of morphology on the charge storage ability, J. Alloys Compd. 695 (2017) 114-123.

[37] Y. Fan, X. Zhang, Y. Liu, Q. Cai, J. Zhang, One-pot hydrothermal synthesis of Mn_3O_4/graphene nanocomposite for supercapacitors, Mater. Lett. 95 (2013) 153-156.

Figure captions

Fig. 1. Rietveld refined XRD patterns of (a) single phase sample, (b) composite sample (Black dots: experimental data; red lines: calculated patterns; blue lines: difference patterns).

Fig. 2. FT-IR spectra of (a) Mn_3O_4 nanostructures and (b) $ZnMn_2O_4/Mn_3O_4$ composite nanostructures.

Fig. 3. (a) FE-SEM image of Mn_3O_4 nanostructures, (b and c) FE-SEM images of $ZnMn_2O_4/Mn_3O_4$ composite nanostructures, (d) BSE image of $ZnMn_2O_4/Mn_3O_4$ composite nanostructures.

Fig. 4. Diameter size distribution histogram of $ZnMn_2O_4/Mn_3O_4$ composite: (a) nanoparticles and (b) nanorods.

Fig. 5. TEM images of $ZnMn_2O_4/Mn_3O_4$ composite nanostructures: (a) low magnification and (b) high magnification.

Fig. 6. EDS spectra of (a) Mn_3O_4 nanostructures and (b) $ZnMn_2O_4/Mn_3O_4$ composite nanostructures.

Fig. 7. (a) CV curves of Mn_3O_4 and $ZnMn_2O_4/Mn_3O_4$ electrodes at the scan rate of 10 mV/s in 1.0 M Na_2SO_4 electrolyte, (b) CV curves of Mn_3O_4 electrode at different scan rates of 1 to 50 mV/s, (c) CV curves of $ZnMn_2O_4/Mn_3O_4$ composite electrode at different scan rates of 1 to 50 mV/s, (d) Variations in the specific capacitance of Mn_3O_4 and $ZnMn_2O_4/Mn_3O_4$ electrodes at different scan rates derived from CV.

Fig. 8. (a) Charge-discharge curves of Mn_3O_4 and $ZnMn_2O_4/Mn_3O_4$ electrodes at 1 A/g current density, (b) Charge-discharge curves of Mn_3O_4 at different current densities from 0.5 to 10 A/g, (c) Charge-discharge curves of $ZnMn_2O_4/Mn_3O_4$ composite at different current densities of 0.5 to 10 A/g, (d) Ragone plots of the Mn_3O_4 and $ZnMn_2O_4/Mn_3O_4$ electrodes.

Fig. 9. (a) Cycle stability of Mn_3O_4 and $ZnMn_2O_4/Mn_3O_4$ electrodes over 2000 cycles, (b) Nyquist plots of Mn_3O_4 and $ZnMn_2O_4/Mn_3O_4$ electrodes in 1.0 M Na_2SO_4 electrolyte and its equivalent circuit model.

Table 1: Crystallite size, degree of crystallinity and Rietveld refinement parameters.

Sample code	Mn^{2+}: Zn^{2+}	Crystalline phase	Composition (%)	Crystallite size(nm)	Degree of crystallinity (%)	R_{wp}	χ^2
S1	100:0	Mn_3O_4	100	21.76	32.63	0.14	1.43
S2	100:10	Mn_3O_4 $ZnMn_2O_4$ λ-MnO_2	90.41 8.25 1.34	24.57 22.98 26.86	55.70	0.12	1.13

Table 2: Comparison of the synthesis route and electrochemical performance of Mn_3O_4 or composite electrodes for supercapacitor applications.

Working electrode	Fabrication method	Potential window (V)	C_S (F/g)	CS retention (%) /cycle number	R_{ct} (Ω)	Ref.
Mn_3O_4/Ni foam composites	hydrothermal	1.0	263	80/2000	NR	[14]
Mn_3O_4	solvothermal	0.95	302	89/5000	0.52	[15]
Mn_3O_4/MnOOH nanocomposite	sonochemical	1.0	307.8	98/2000	4.34	[17]
MoS_2/Mn_3O_4	hydrothermal and chemical precipitation	0.4	172.2	69.3/2000	1.41	[30]
Mn_3O_4	low temperature solution process	2.0	216	85/1000	4.30	[31]
rGO-Mn_3O_4 composites	atom-efficient strategy	1.0	221.6	97.1/1000	NR	[32]
Mn_3O_4/graphene	hydrothermal	1.0	171	NR	NR	[37]
$ZnMn_2O_4/Mn_3O_4$ composites	electrochemical deposition	1.0	321.3	93/2000	0.76	This work

NR: not reported

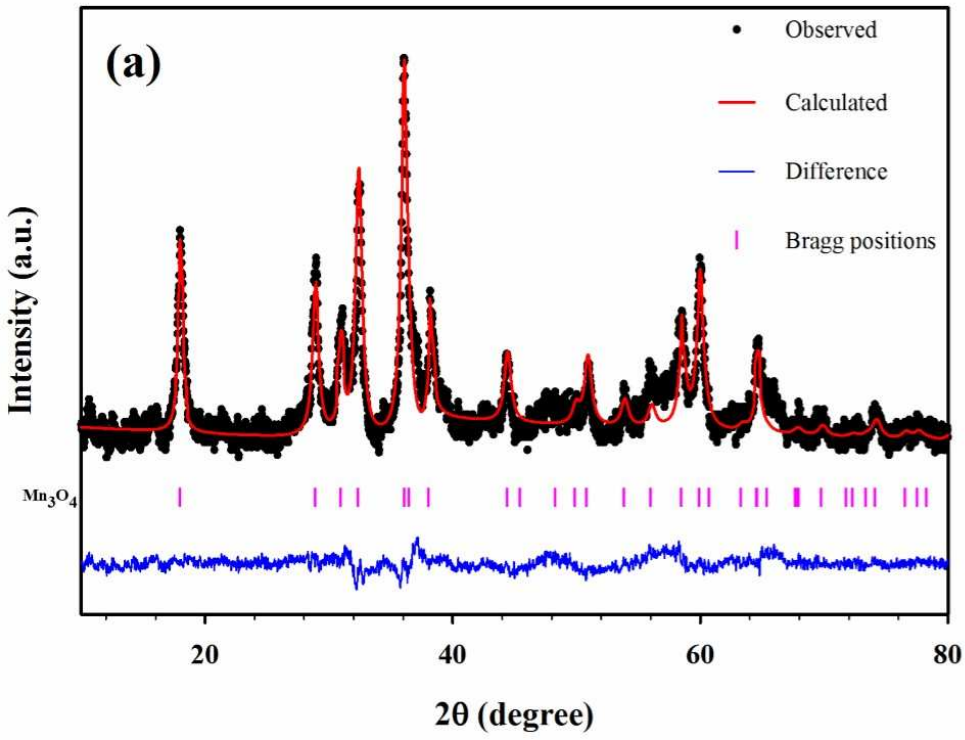
(a)
Observed
Calculated
Difference
Bragg positions
Intensity (a.u.)
Mn_3O_4
20
40
60
80
2θ (degree)

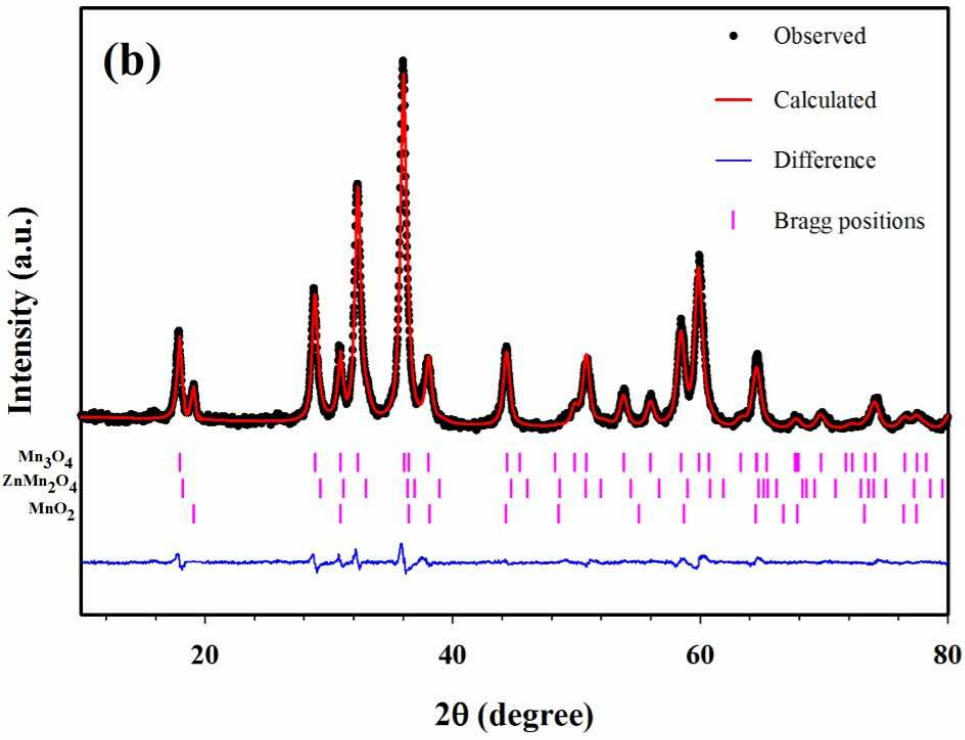
(b)
Observed
Calculated
Difference
Bragg positions
Intensity (a.u.)
Mn_3O_4
$ZnMn_2O_4$
MnO_2
20
40
60
80
2θ (degree)

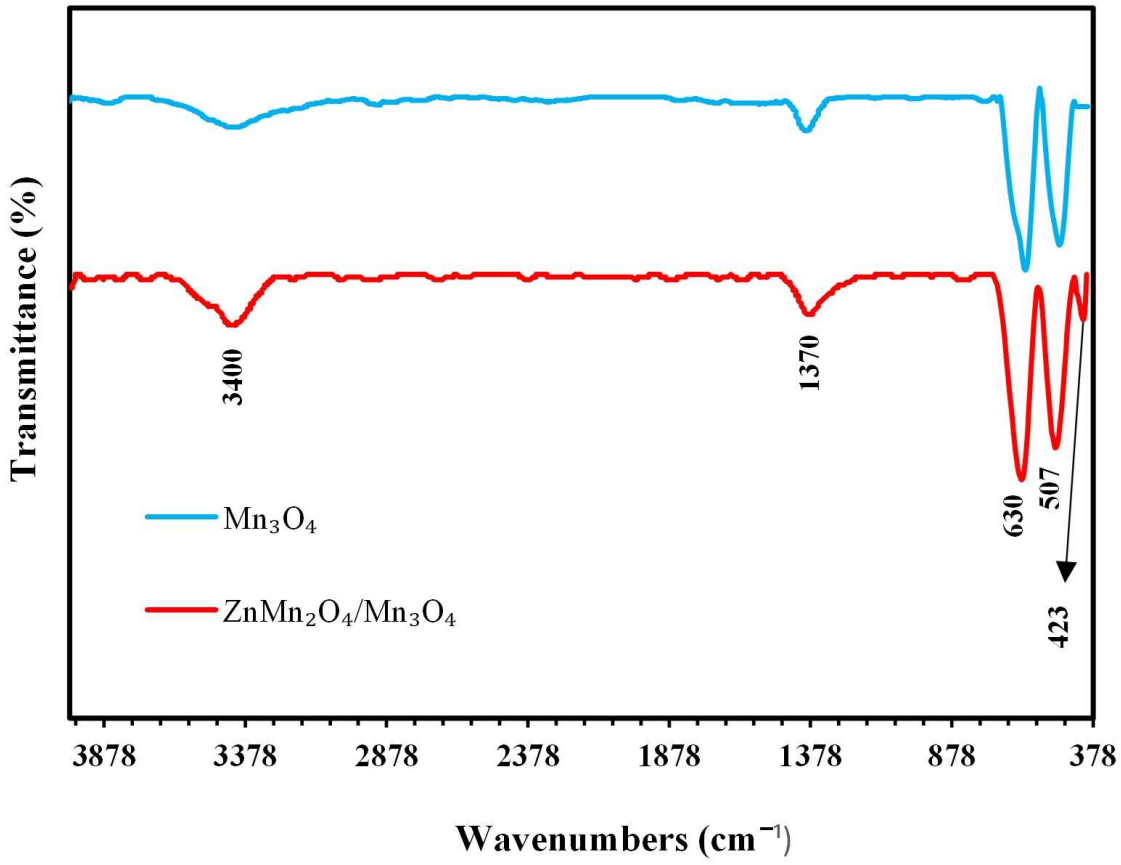

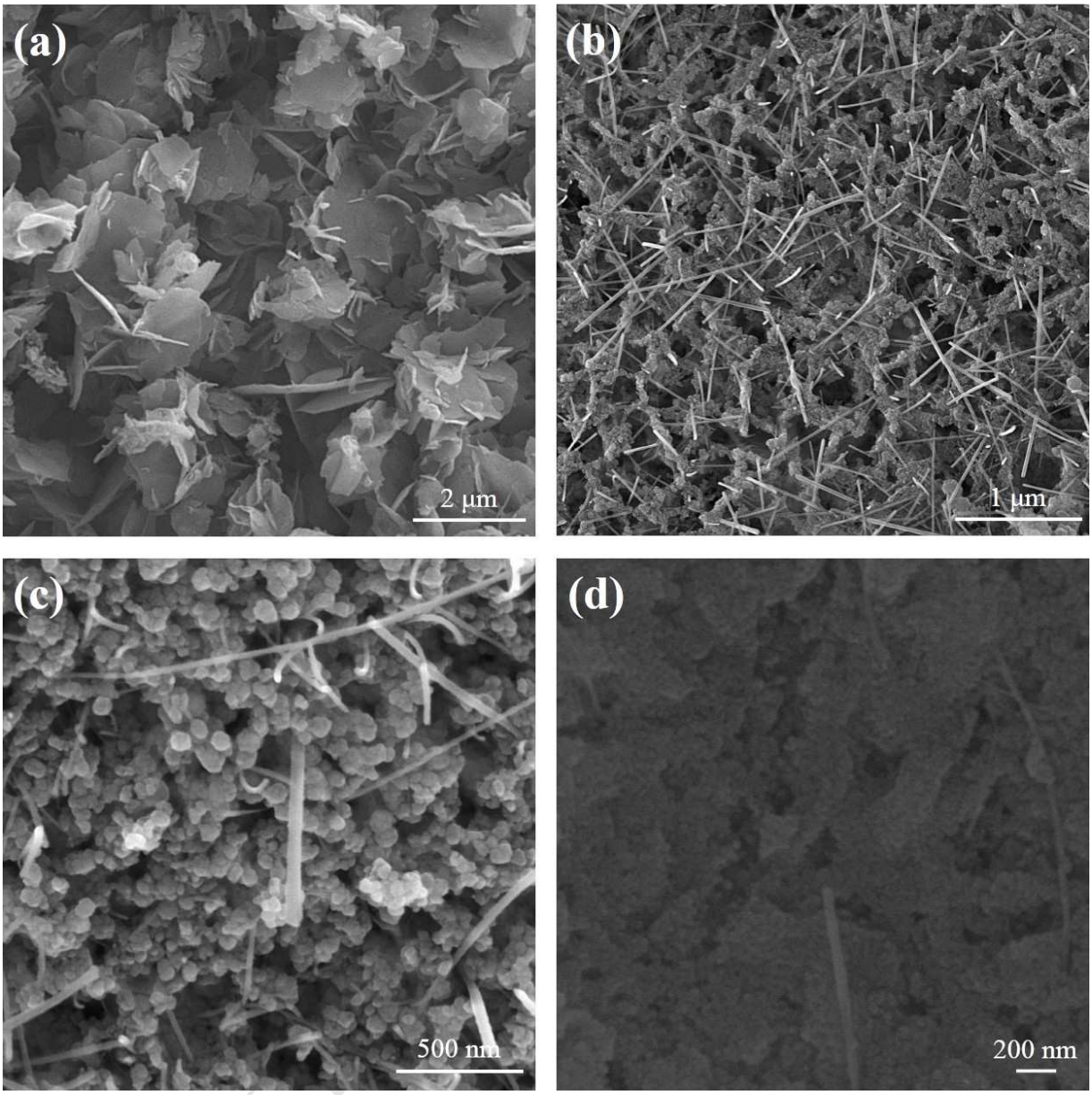

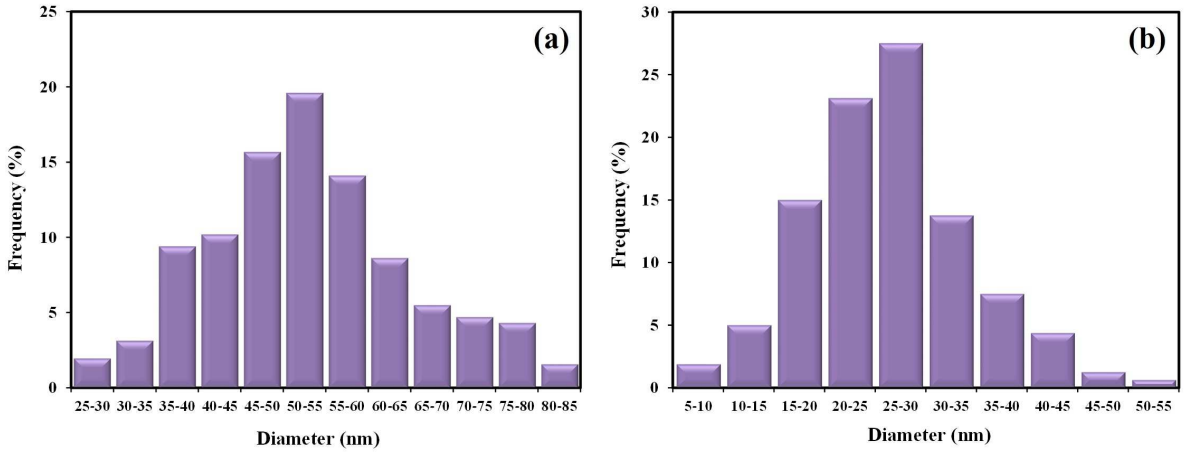

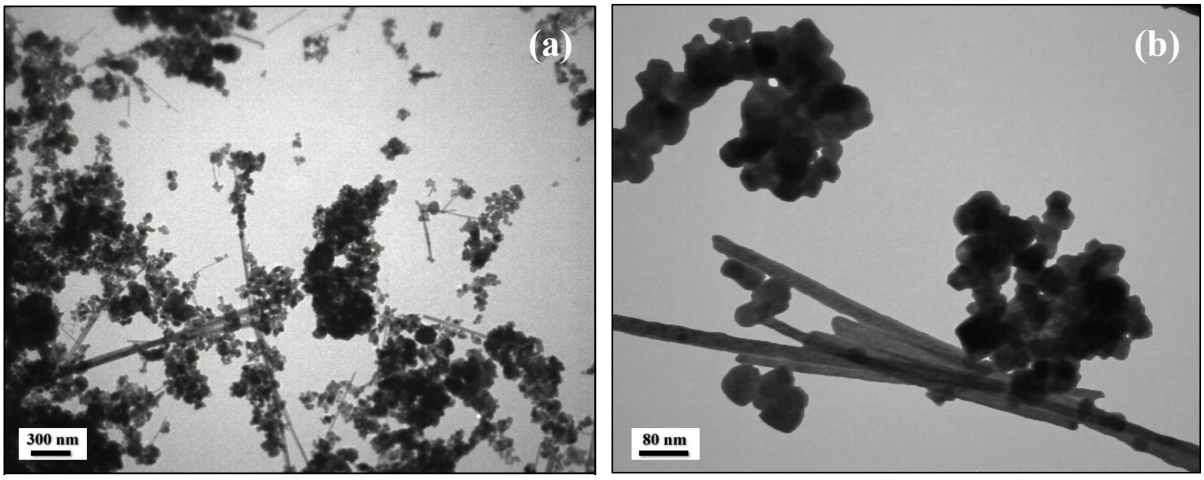

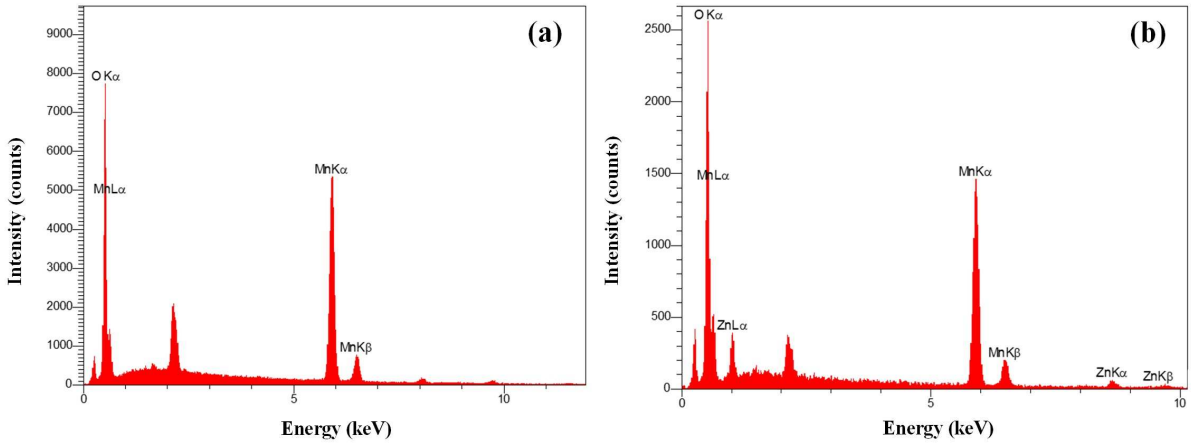

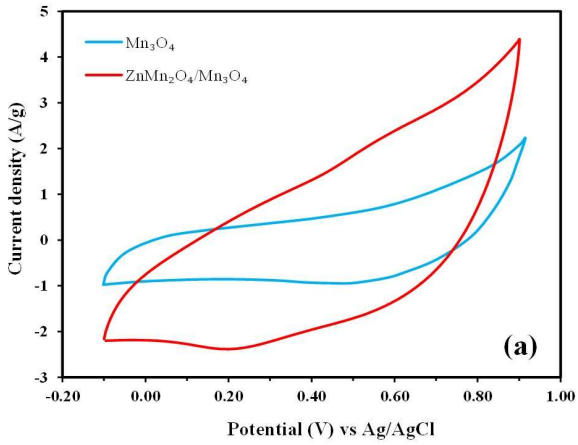
Mn3O4
ZnMn2O4/Mn3O4
Current density (A/g)
Potential (V) vs Ag/AgCl
(a)

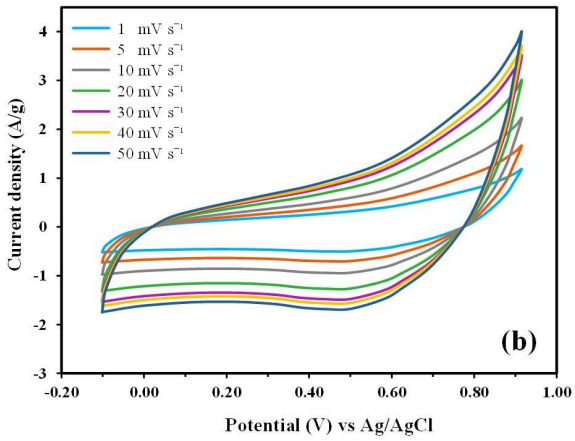
1 mV s-1
5 mV s-1
10 mV s-1
20 mV s-1
30 mV s-1
40 mV s-1
50 mV s-1
Current density (A/g)
Potential (V) vs Ag/AgCl
(b)

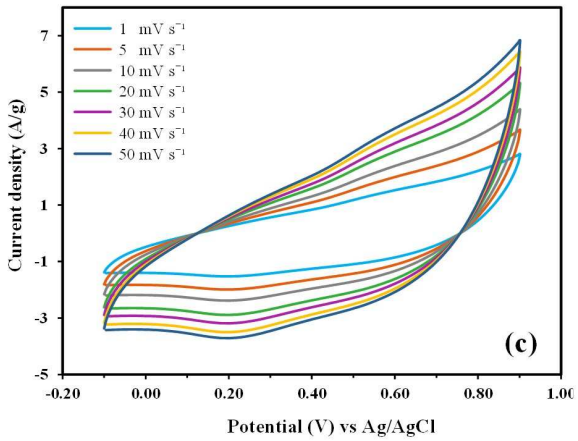
1 mV s-1
5 mV s-1
10 mV s-1
20 mV s-1
30 mV s-1
40 mV s-1
50 mV s-1
Current density (A/g)
Potential (V) vs Ag/AgCl
(c)

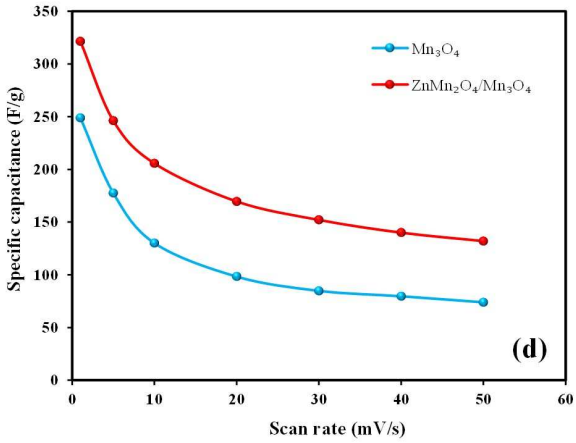
Mn3O4
ZnMn2O4/Mn3O4
Specific capacitance (F/g)
Scan rate (mV/s)
(d)

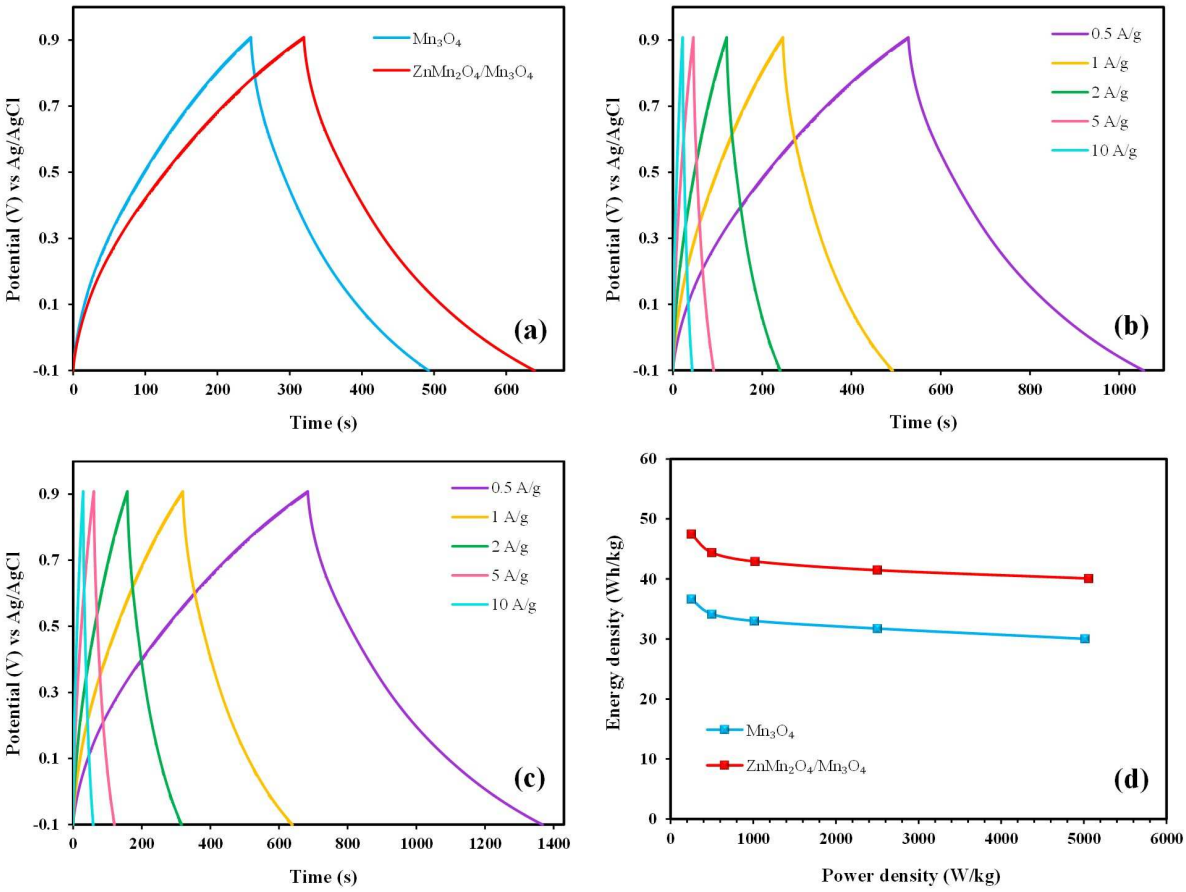

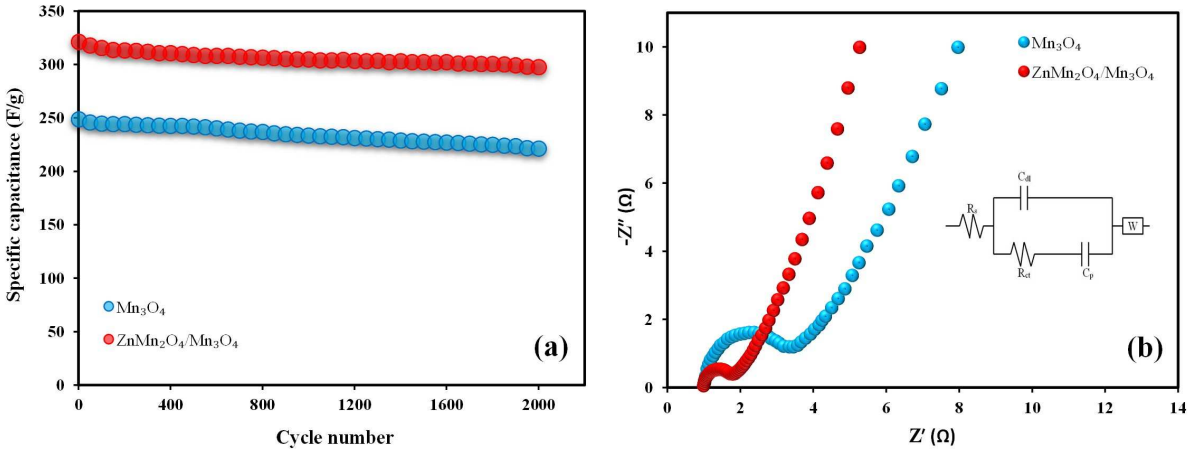

Highlights

- $ZnMn_2O_4/Mn_3O_4$ composite was synthesized by cathodic electrodeposition.
- The prepared composite possess nanosized rod/particle morphology.
- The prepared composite nanostructure exhibited a maximum storage capacity of 321.34 Fg^{-1}.